Photon yield of superradiant inverse Compton scattering from microbunched electrons

PAPER • OPEN ACCESS

Photon yield of superradiant inverse Compton scattering from microbunched electrons

To cite this article: B H Schaap *et al* 2022 *New J. Phys.* **24** 033040

New Journal of Physics
The open access journal at the forefront of physics

Deutsche Physikalische Gesellschaft DPG
IOP Institute of Physics

Published in partnership with: Deutsche Physikalische Gesellschaft and the Institute of Physics

OPEN ACCESS

RECEIVED
15 November 2021

REVISED
4 February 2022

ACCEPTED FOR PUBLICATION
2 March 2022

PUBLISHED
28 March 2022

PAPER

Photon yield of superradiant inverse Compton scattering from microbunched electrons

B H Schaap[1,*], T D C de Vos[1], P W Smorenburg[2] and O J Luiten[1]

[1] Department of Applied Physics, Eindhoven, Eindhoven University of Technology, PO Box 513, 5600 MB Eindhoven, The Netherlands
[2] ASML Netherlands B.V., PO Box 324, 5500 AH Veldhoven, The Netherlands
[*] Author to whom any correspondence should be addressed.

E-mail: b.h.schaap@tue.nl

Keywords: inverse Compton scattering, compact x-ray sources, microbunching, superradiant emission

Abstract

Compact x-ray sources offering high-brightness radiation for advanced imaging applications are highly desired. We investigate, analytically and numerically, the photon yield of superradiant inverse Compton scattering from microbunched electrons in the linear Thomson regime, using a classical electrodynamics approach. We show that for low electron beam energy, which is generic to inverse Compton sources, the single electron radiation distribution does not match well to collective amplification pattern induced by a density modulated electron beam. Consequently, for head-on scattering from a visible laser, the superradiant yield is limited by the transverse size of typical electron bunches driving Compton sources. However, by simultaneously increasing the electron beam energy and introducing an oblique scattering geometry, the superradiant yield can be increased by orders of magnitude.

1. Introduction

Radiation in the soft and hard x-ray regime has become an indispensable tool for application in life and material sciences [1]. Free electron lasers (FELs) offer coherent x-ray pulses of unprecedented high brightness, however, these machines are only available at specialized, costly large scale facilities [2, 3]. Development of laboratory scale x-ray sources is therefore highly desirable. A promising approach for generating x-rays in a compact setup is inverse Compton scattering (ICS), in which an electron beam colliding with a laser pulse produces radiation. Due to the short wavelength of the laser pulse (compared to an undulator), the beam energy required to generate x-rays can be reached with table-top accelerators. Several ICS-sources are in construction or operational today [4–8]. The drawback of ICS is, however, that the conversion from driving laser to x-ray photons is rather low.

In a FEL, the incoherent undulator radiation initiates a periodic density modulation process that bunches the electron beam with a period on the scale of the radiation wavelength. The introduced microbunching make the electrons radiate collectively, leading to coherent amplification of the radiation, also known as superradiance [9, 10], which exponentially increases the FEL yield. This so-called self-amplified spontaneous emission (SASE) process could also be initiated by x-rays from incoherent ICS [11–13], but due to the stringent requirements on laser and electron beam parameters has yet to be demonstrated experimentally.

Alternatively, the superradiant yield can be enhanced by imposing density modulation before the x-ray emission process [14, 15]. In FELs, prebunching is attained by schemes like high-gain high harmonic generation [16–18] and echo-enabled harmonic generation [19–21], mainly for greater longitudinal coherence and shorter saturation length. At low beam energies, several prebunching methods have been proposed: transverse modulation attained by masking or diffraction on a crystalline solid is transported trough an emittance exchange line that converts the transverse modulation to a longitudinal modulation [14, 15, 22]. Another method is to impart an energy modulation that converts into a density modulation by

velocity bunching. The modulation can be realized by either the two-color ponderomotive force [23], the inverse FEL process [24] or by time varying electric fields [25, 26]. Also, microbunched electrons can be generated at the source by photoemission from shaped laser pulses [27] or periodically modulated ionization of a laser cooled gas [28, 29]. Each method offers varying modulation period and compatibility with beam energy and might require further compression or beam manipulation to reach modulation at x-ray frequencies.

All of these prebunching techniques rely on the assumption that a density modulation leads to significant coherent amplification of the single-electron radiation distribution. However, in this paper we will show that the induced superradiance is highly angularly dependent, and does not necessarily match well to the angular dependence of the single-electron radiation pattern. Especially at the low beam energies (few to tens of MeVs) relevant for x-ray ICS sources, this mismatch can lead to a reduction in superradiant flux of many orders of magnitude compared to a fully superradiant beam.

Here, a formalism is provided for calculating the number of superradiant photons from ICS by microbunched electrons. The resulting expressions can be used as a tool for designing a coherent Compton x-ray source driven by a prebunched electron beam. The paper is organized as follows: first, in section 2, we introduce some basic properties of ICS. Second, in section 3, we discuss the essential components of the three dimensional model of superradiant ICS: the single electron radiation distribution describing the spectral angular properties of the scattering process and the three dimensional bunching factor, which describes the full spectral angular dependence of collective emission by an electron bunch. Third, in section 4 we combine the single electron radiation distribution with the bunching factor to calculate the yield of superradiant photons from a cold modulated Gaussian electron bunch for head-on and non-collinear scattering. Then, we estimate the effects of finite energy spread and emittance on the superradiant yield. Last, we apply the derived expression to a proposed coherent soft x-ray source.

2. Basic properties of ICS

When a laser pulse collides with a relativistic electron (see figure 1(a)), the wavenumber of the scattered radiation is increased due to the relativistic Doppler shift. The increase in wavenumber is described by the well-known expression

$$k_1 = k_0 \frac{1 - \mathbf{n}_0 \cdot \mathbf{v}/c}{1 - \mathbf{n} \cdot \mathbf{v}/c}, \tag{1}$$

where k_0 the wavenumber of the laser pulse, $\mathbf{v}$ the velocity vector of the electron, c the speed of light, $\mathbf{n}_0 = \mathbf{k}_0/k_0$ and $\mathbf{n} = \mathbf{k}/k$ are unit vectors pointing in the propagation direction of the laser pulse and scattered radiation, respectively. The scattered frequency (1) is strongly angular dependent: it is highest along the propagation direction of the electron $\theta = \arccos(\mathbf{n} \cdot \mathbf{v}/v) = 0$, and becomes progressively lower at larger scattering angles.

Also the radiation distribution of ICS is highly angular dependent: it is well known from classical electrodynamics [30] that an ultrarelativistic electron that is accelerated perpendicular to its velocity mostly radiates into a cone of half angle $\Theta \simeq 1/\gamma$, where $\gamma = \sqrt{1 - v^2/c^2}$ the Lorentz factor, with symmetry axis along its propagation direction. Within a small bandwidth $\delta k/k \ll 1$ around the on-axis frequency, the opening angle (see figure 1(b)) is approximately given by [31]

$$\Theta_1 = \frac{1}{\gamma}\sqrt{\frac{\delta k}{k}}, \tag{2}$$

which can also be found directly from (1) in the ultrareltivistic limit $\gamma \gg 1$. For incoherent ICS sources with unmodulated electron bunches, Θ_1 is the smallest possible half angle in which all radiation is contained.

The number of photons within angle Θ_1 scattered by an unmodulated electron bunch of N_e electrons from a laser pulse having $N_\phi = k_0\sigma_z$ number of periods with σ_z the rms pulse length, is given by [31, 32]

$$N_{\mathrm{ph}}^{\mathrm{inc}} = \frac{\pi}{4}\alpha A_0^2 N_\phi N_e \frac{\delta k}{k}, \tag{3}$$

where α the fine-structure constant, $A_0 = eE_0/(m_e c^2 k_0)$ the normalized vector potential of the laser and E_0 the laser electric field amplitude, m_e the electron mass and c the speed of light. In (3) it is assumed that the waist of the electron beam is much smaller than the waist of the laser pulse. Furthermore, the linear Thomson regime is assumed, i.e. $A_0 \ll 1$, such that spectral broadening due to nonlinear effects is negligible [33]. Without appropriately chirping the laser frequency [34–37], the non-linear effects limit

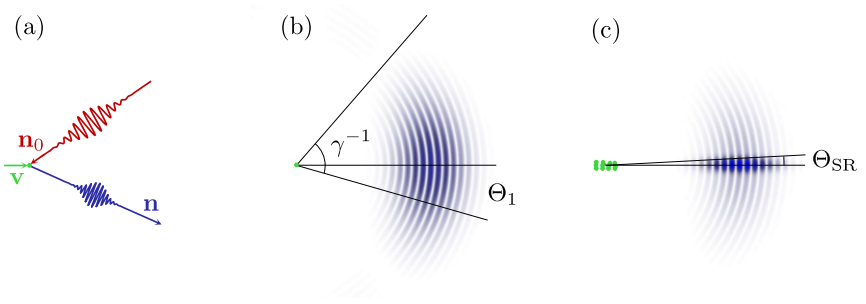

Figure 1. (a) ICS geometry. (b) Single electron radiation intensity. (c) Superradiant ICS from a density modulated electron bunch.

upscaling of the photon yield with laser intensity. To certain extent, the yield can be linearly increased by interaction length [13] or by charge [38, 39].

Alternatively, the yield can be scaled up by imparting a modulation to the charge density distribution. If the modulation period is resonant with the scattered radiation, such that the individual microbunches radiate in phase with the others, the yield will scale quadratically with charge. In the ideal case, all scattered radiation within a bandwidth $\delta k/k = 1/N_\mathrm{b}$ defined by the number of microbunches N_b, will be coherently amplified, such that the yield is given by:

$$N_{\mathrm{ph,\,1D}}^{\mathrm{SR}} = \frac{\pi}{4}\alpha A_0^2 N_\phi N_\mathrm{e}^2 b_1^2 \frac{1}{N_\mathrm{b}}, \tag{4}$$

where $b_1 = \int_{-\infty}^{\infty}\Lambda(z)\exp[-i\Delta\varphi]\mathrm{d}z \in [0,1]$ the one-dimensional bunching factor with $\Lambda(z)$ the line density of the microbunched electrons and $\Delta\varphi \simeq kz$ the phase difference measured by the central amplified wavenumber k. The bunching factor is a measure for the quality of modulation: if $b_1 = 0$ the bunch is unmodulated, if $b_1 = 1$ the modulation is ideal. When the latter is true, even for moderate bunch charges $N_\mathrm{e} = 10^6$, the yield is significantly enhanced with respect to the incoherent part $N_\mathrm{ph}^{\mathrm{inc}}$.

However, in contrast to the incoherent radiation, if the electron bunch is modulated, the superradiant emission can be confined to an even smaller angle than Θ_1 see figure 1(c). The finite transverse waist of the modulated electron bunch limits the amplification to a certain angle at which the single-electron emission starts to interfere destructively. For an electron beam waist $\sigma_\perp$, the opening angle of the superradiant cone can be expected to be on the order of [40, 41]

$$\Theta_{\mathrm{SR}} = \frac{1}{k\sigma_\perp}. \tag{5}$$

This angle coincides with the well-known divergence angle of the fundamental transverse (TEM_{00}) Gaussian mode, which is also the dominant mode amplified in SASE FELs [42].

The main problem we will address in this paper is that for low electron beam energies (few to tens of MeV), generic to x-ray ICS sources, the superradiant angle Θ_{SR} is much smaller than the single emission angle Θ_1 and thus equation (4) does not hold. For example, to generate $\lambda = 1.24$ nm (photon energy $U_\mathrm{ph} = 1$ keV) x-rays by head-on collision with a laser pulse of wavelength $\lambda_0 = 1$ μm, an electron bunch is required with kinetic energy $U_\mathrm{kin} = (\gamma - 1)m_\mathrm{e}c^2 = 6.8$ MeV, corresponding to $\gamma = 14$. The single electron opening angle for these x-rays within a 1% bandwidth $\Theta_1 \simeq 7.1$ mrad. Assuming an electron bunch waist size of $\sigma_\perp = 5$ μm, which is small compared to typical ICS-sources [4–8], the superradiant angle is $\Theta_{\mathrm{SR}} \simeq 39$ μrad, more than two orders of magnitude smaller than Θ_1. As such, only a small part of the single electron radiation is coherently amplified. Thus, for a correct description of superradiant ICS, we have to take into account the transverse degrees of freedom of the electron bunch, which will be done in the next section.

3. Three dimensional theory of superradiant ICS

In what follows, we will formulate a set of expressions that quantify the number of superradiant photons that is generated by ICS from a three dimensional, density modulated electron bunch. For ICS, or any other electron bunch induced radiation process, the radiation distribution, i.e. the total amount of photons that is emitted per unit solid angle and per unit spatial frequency, by a general electron bunch with N_e electrons can be written as [40, 43]:

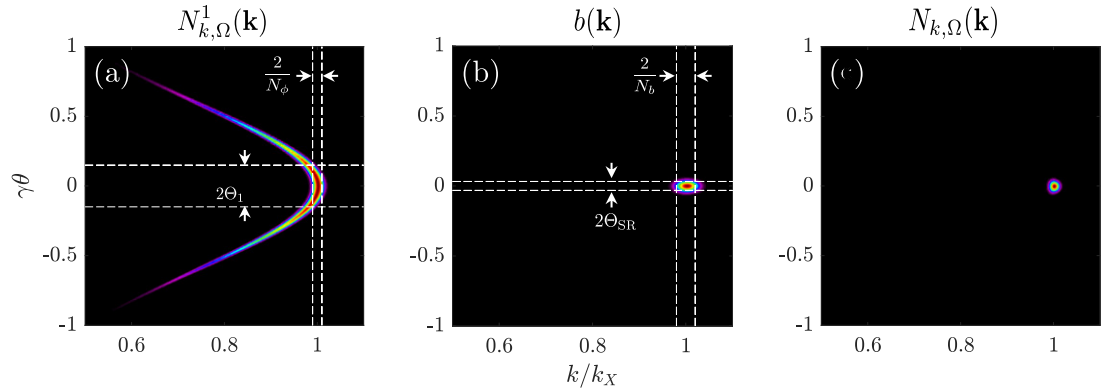

Figure 2. Head-on scattering: (a) single electron radiation distribution. (b) Bunching factor of a modulated Gaussian. (c) Resulting full radiation distribution of the superradiant emission.

$$N_{k,\Omega}(\mathbf{k}) = N^1_{k,\Omega}(\mathbf{k}) \times [N_e + N_e(N_e - 1)|b(\mathbf{k})|^2], \tag{6}$$

where $N^1_{k,\Omega}(\mathbf{k}) = \mathrm{d}^2N^1_{\mathrm{ph}}/(\mathrm{d}\Omega\,\mathrm{d}k)$ is the single electron radiation distribution and $b(\mathbf{k}) \in [0, 1]$ is the three dimensional bunching or coherence factor describing the phase correlations of the generated radiation. The first part of this equation, scaling linearly with the amount of electrons N_e, is the incoherent contribution of the radiation. The second part, scaling with N_e^2, describes the coherent radiation, which is the dominant term when $N_e \gg 1$ and $b(\mathbf{k}) \simeq 1$.

Although single electron radiation distributions $N^1_{k,\Omega}(\mathbf{k})$ have been calculated by numerous authors before [31, 32, 44, 45], we have provided a compact derivation in appendix A to make this work self-contained. The single electron radiation distribution for collision with a linearly polarized Gaussian plane wave is given by:

$$N^1_{k,\Omega}(\mathbf{k}) = \frac{\alpha A_0^2 N_\phi^2}{4\pi}\frac{k}{\kappa_0^2}\left[1 - \frac{(\mathbf{k}\cdot\hat{\boldsymbol{\epsilon}})^2}{\kappa_0^2}\right]\exp\left[-N_\phi^2\left(1 - \frac{k}{k_1}\right)^2\right], \tag{7}$$

where N_ϕ is the number of periods of the laser, A_0 the normalized vector potential laser amplitude, $\kappa_0 = \gamma k_0(1 - \mathbf{n}_0\cdot\mathbf{v}/c)$ the wavenumber of the laser in the rest frame of the electron, $\hat{\boldsymbol{\epsilon}}$ is the polarization vector of the laser, which in (7) is assumed to be perpendicular to $\mathbf{v}$. The exponential term is the so-called resonance function [31] which peaks at wavenumber k_1. The bandwidth of the resonance function is determined by the finite length of the drive laser pulse. When evaluated at k_1, the first term between square brackets describes the angular dependency of the relativistic differential cross-section [45], which is zero at $\theta = \arccos(\beta)$ or $\theta \simeq 1/\gamma$ in the ultrarelativistic limit. The single electron radiation distribution for head-on scattering is plotted in figure 2(a).

The superradiant contribution to the scattered radiation is governed by bunching factor $b(\mathbf{k})$. Provided that all electrons have identical initial velocities, which we will refer to as the cold beam approximation, and assuming we can neglect Coulombic interactions, the bunching factor is written as:

$$b(\mathbf{k}) = \frac{1}{Q}\int_{-\infty}^{\infty}\rho(\mathbf{x})\exp[-i\Delta\varphi]\mathrm{d}^3\mathbf{x}, \tag{8}$$

where $\rho(\mathbf{x})$ is the (continuous) charge density distribution and $Q = -eN_e$ the total charge of the bunch. The argument $\Delta\varphi$ of the complex exponential measures the phase difference between electrons separated by $\mathbf{x}$, which can be written as:

$$\Delta\varphi = \mathbf{k}\cdot\mathbf{x} - \frac{k}{k_1}\mathbf{k}_0\cdot\mathbf{x}, \tag{9}$$

where $\mathbf{k}\cdot\mathbf{x}$ is the phase difference due to the geometric separation between the electrons. The second term results from the finite phase velocity of light, which we will explain using figure 3, where two electrons (I and II in green) moving at velocity $\mathbf{v}_0$ are shown in the comoving frame. Reference electron I is positioned at the origin and electron II at some arbitrary constant vector $\mathbf{x}$. The phase difference along the scattering direction $\mathbf{n}$ due to distance between the electrons is evidently $\mathbf{k}\cdot\mathbf{x}$, giving us the first term in equation (9). After passing electron I, the driving laser's wavefront (in red) has to travel a optical path length $\mathbf{n}_0\cdot\mathbf{x}$ to reach electron II, which takes time $\tau = \mathbf{n}_0\cdot\mathbf{x}/v_{\mathrm{p},0}$, with $v_{\mathrm{p},0} = c - \mathbf{n}_0\cdot\mathbf{v}$ the phase velocity of the laser in the comoving frame. During time τ the scattered radiation leaving I and propagating at phase

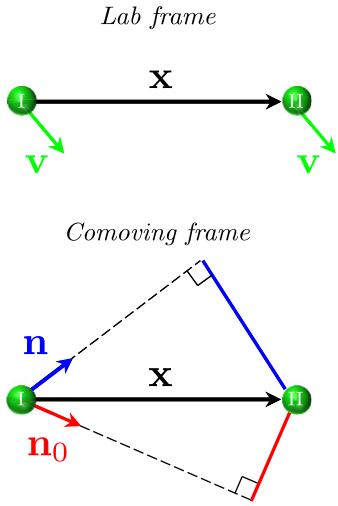

Figure 3. Two electrons in the lab frame and comoving frame scattering radiation (blue) from driving laser (red).

velocity $v_\mathrm{p} = c - \mathbf{n}\cdot\mathbf{v}$, has traveled a path length $\Lambda = \mathbf{n}_0\cdot\mathbf{x}v_\mathrm{p}/v_{\mathrm{p},0}$, which is then subtracted from the geometrical path length difference, resulting in the sought after expression. Therefore, if the scattered radiation and laser are copropagating this decreases the phase difference; when they are counterpropagating first electron II will be reached by the laser, and the sign of Λ changes, increasing the phase difference. The phase difference (9) can also be found directly by rewriting equation (A.5).

For the calculations below we will use a cold Gaussian, cylindrically symmetric distribution of charge with a periodic modulation along modulation wavevector $\mathbf{k}_\mathrm{e}$, which in terms of its Fourier components is given by:

$$\rho(\mathbf{x}) = \rho_0 \sum_{n=-\infty}^{\infty} b_n \exp\left[-\frac{1}{2}\mathbf{x}^\mathrm{T}\mathcal{S}^{-1}\mathbf{x} + in\mathbf{k}_\mathrm{e}\cdot\mathbf{x}\right], \tag{10}$$

where $\rho_0 = -eN_\mathrm{e}\left[\sum_{n=-\infty}^{\infty} b_n \exp\left(-n^2N_\mathrm{b}^2/2\right)\right]^{-1}\left[(2\pi)^3 \det\,\mathcal{S}\right]^{-1/2}$ the peak charge density, variance matrix $\mathcal{S} = \mathrm{diag}(\sigma_\perp^2, \sigma_\perp^2, \sigma_\parallel^2)$, $N_\mathrm{b} = (\mathbf{k}_\mathrm{e}^\mathrm{T}\mathcal{S}\mathbf{k}_\mathrm{e})^{1/2}$ is the number of microbunches and $\sigma_\perp$ and $\sigma_\parallel$ the transverse and longitudinal rms waist size of the electron bunch. The Fourier coefficient b_n of the nth harmonic is:

$$b_n = \frac{1}{2\pi}\int_0^{2\pi} w(\mathbf{k}_\mathrm{e}\cdot\mathbf{x}) \exp\left[-in\mathbf{k}_\mathrm{e}\cdot\mathbf{x}\right] \mathrm{d}(\mathbf{k}_\mathrm{e}\cdot\mathbf{x}), \tag{11}$$

where $w(x) > 0$ describes an arbitrary periodic density modulation, which is normalized such that the zero frequency component $b_0 = 1$. In the case of cosine modulation $w(x) = 1 + \cos(x)$, only b_0 and the fundamental orders $b_{\pm1} = 1/2$ contribute to the expansion. However, for an ideal Dirac comb $w(x) = \sum_{m=-\infty}^{\infty}\delta(x - m2\pi)$, with $\delta(x)$ the Dirac delta function, all higher harmonics $n > 1$ contribute equally, $b_n = 1$, to the Fourier expansion of the density modulation. Strong harmonic content of the bunching frequency is also found in more complex density modulation, for example attained in schemes like high-gain high harmonic generation [16–18] and echo-enabled harmonic generation [19, 20].

Combining equations (8)–(10), and assuming $N_\mathrm{b} \gg 1$ such that the exponent in the denominator in ρ_0 is negligible, the bunching factor for positive frequencies without the zero-frequency band is given by

$$b(\mathbf{k}) = \sum_{n=1}^{\infty} b_n \exp\left[-\frac{1}{2}\bar{\mathbf{k}}_n^\mathrm{T}\mathcal{S}\bar{\mathbf{k}}_n\right], \tag{12}$$

where $b_n \in [0, 1]$ the Fourier coefficients of the density modulation, which describe the maximum bunching amplitude of the nth harmonic of k_e, and $\bar{\mathbf{k}}_n = \mathbf{k} - k/k_1\mathbf{k}_0 - n\mathbf{k}_\mathrm{e}$ with k_1 given by equation (1). Bunching factor (12) describes the spectral angular characteristics of the induced superradiance by a Gaussian charge distribution with an arbitrary periodic density modulation for arbitrary scattering geometry. In figure 2(b) the ($n = 1$) bunching factor (12) is shown for head-on scattering.

In the next section we will consider specific cases of (12) and for those cases calculate the superradiant yield. Although the main properties remain the same, other envelope distributions can be used.

4. Superradiant x-ray yield

The single electron radiation distribution (7) and bunching factor (12), are now combined to calculate, numerically and analytically, the total superradiant yield for different scattering geometries by evaluating the following integral

$$N_{\mathrm{ph}}^{\mathrm{SR}} = \int \mathrm{d}\Omega \int N_{\mathrm{e}}^2 N_{k,\Omega}^1(\mathbf{k}) |b(\mathbf{k})|^2 \mathrm{d}k, \tag{13}$$

with $\mathrm{d}\Omega = \sin\theta\, \mathrm{d}\theta\, \mathrm{d}\phi$. Here, it was assumed that $N_{\mathrm{e}} \gg 1$ such that $N_{\mathrm{e}}(N_{\mathrm{e}} - 1) \simeq N_{\mathrm{e}}^2$, and that the electron bunch propagates along the z-axis. In the following, we will only consider superradiance due the fundamental of the bunching frequency ($n = 1$), which can be trivially extented to higher harmonics *a posteriori*. The superradiant photon yield $N_{\mathrm{ph}}^{\mathrm{SR}}$ from this three dimensional study is compared to the ideal one dimensional case. To this end, we introduce the efficiency of the superradiant yield, defined by:

$$\eta = \frac{N_{\mathrm{ph}}^{\mathrm{SR}}}{N_{\mathrm{ph,\,1D}}^{\mathrm{SR}}}, \tag{14}$$

with $N_{\mathrm{ph,\,1D}}^{\mathrm{SR}} = \frac{\pi}{4}\alpha A_0^2 N_\phi N_{\mathrm{e}}^2 b_1^2 / N_{\mathrm{b}}$ the one-dimensional superradiant yield (4) and b_1 is the maximum of the on-axis bunching factor. If $\eta = 1$ the single electron emission is completely amplified by the modulated electron bunch, which radiated as a one-dimensional pencil beam. If $\eta < 1$, the coherent amplification is not completely utilized as a result of destructive interference from the finite transverse size of the electron bunch.

In the following, we first discuss the head-on scattering geometry. Then, in section 4.2 also the superradiant yield for non-collinear scattering is discussed.

4.1. Head-on scattering

Experimentally, the most common configuration is head-on scattering in which the electrons bunch generates x-rays from a counterpropagating laser pulse [4–8]. In this configuration, the Doppler shift is maximized, yielding the largest scattered wavenumber $k_X = k_0(1+\beta)/(1-\beta)$ for a particular electron beam energy, where $\beta = v/c$.

In the head-on geometry, the bunching factor $b(\mathbf{k})$ for a modulated Gaussian electron bunch with bunching wavevector along its propagation axis $\mathbf{k}_{\mathrm{e}} = k_{\mathrm{e}}\mathbf{e}_z$ has significant superradiant emission along the axis ($\theta = 0$) if $k_{\mathrm{e}} = 2k_0/(1-\beta)$. The bunching wavenumber k_{e} is larger than the resonant on-axis radiation wavenumber k_X due to the finite propagation speed of the scattered radiation and laser driving the scattering process. For these parameters, equation (12) also confirms that a large bunching factor, and hence significant coherence, the emission is confined to a central cone of angle $\Theta_{\mathrm{SR}} = \arcsin\left[1/(\sigma_\perp k)\right]$, which for small angles $\Theta_{\mathrm{SR}} \simeq 1/(\sigma_\perp k)$. As mentioned, the typical transverse waists of electron bunches in ICS sources is several micrometers [4–8], ensuring that Θ_{SR} is small for x-rays.

In the small-angle approximation, integral (13) to calculate the superradiant yield can be performed analytically. For briefness, we divert this part of straightforward but cumbersome calculations to appendix B. We find that the superradiant yield efficiency can be written as:

$$\eta = \mathrm{erfcx}\left(\xi^{-1}\right), \tag{15}$$

where the function $\mathrm{erfcx}(x) = \exp[x^2](1 - 2/\sqrt{\pi}\int_0^x \exp[-y^2]\mathrm{d}y)$ is the scaled complementary error function, and:

$$\xi = \frac{1}{2}\frac{1+\beta}{1-\beta}\frac{1}{k_X^2\sigma_\perp^2}\frac{N_{\mathrm{b}}N_\phi}{\sqrt{N_{\mathrm{b}}^2 + N_\phi^2}} \simeq 2\frac{\Theta_{\mathrm{SR}}^2}{\Theta_1^2}, \tag{16}$$

is the collectivity parameter being a measure for how well the single electron angle Θ_1 and superradiant angle Θ_{SR} overlap. Here, $\Theta_1 \simeq \sqrt{\delta k/k}/\gamma$ with bandwidth $\delta k/k = \sqrt{(\delta k/k)_1^2 + (\delta k/k)_{\mathrm{SR}}^2}$ where $(\delta k/k)_{\mathrm{SR}} = 1/N_{\mathrm{b}}$ and $(\delta k/k)_1 = 1/N_\phi$ are relative bandwidths of the superradiant and single electron spectrum, see figure 2.

As expected, the superradiant emission is suppressed by the transverse degrees of freedom of the electron bunch. It is interesting to investigate how η behaves at limiting values of ξ. For small arguments $x \ll 1$, $\mathrm{erfcx}(x) \simeq 1$; for large arguments $x \gg 1$, $\mathrm{erfcx}(x) \simeq 1/(\sqrt{\pi}x)$. Thus, the superradiant efficiency can be approximated by:

$$\eta = \begin{cases} 1 & \text{for } \xi \gg 1 \\ \dfrac{\xi}{\sqrt{\pi}} & \text{for } \xi \ll 1 \end{cases}, \tag{17}$$

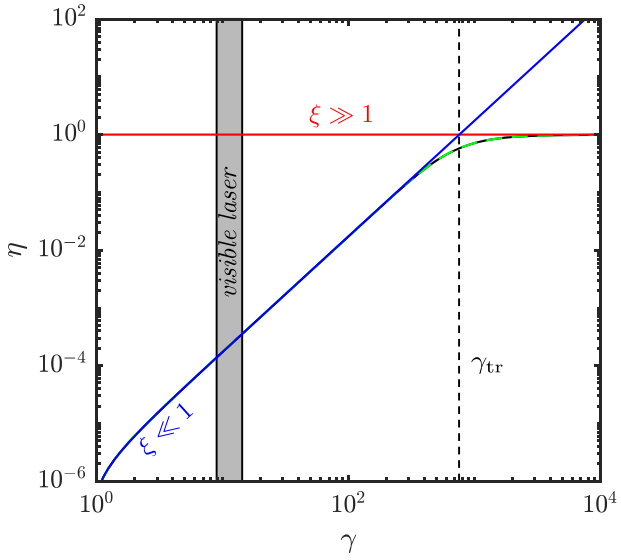

Figure 4. The superradiant yield for head-on scattering as function of electron beam energy. Here, an electron bunch with $\sigma_\perp = 5\ \mu$m and $N_{\rm b} = 10^4$ microbunches scatters $\lambda_X = 1.24$ nm ($U_{\rm ph} = 1$ keV) photons from a pulse of $N_\phi = 10^3$. The grey box corresponds to laser wavelengths in the visible regime (400–1000 nm).

where the first expression corresponds to the pencil beam regime and the second to the beer-can beam regime in which transverse degrees of freedom dominate.

In the pencil beam regime, the opening angle of the superradiant cone is much larger than the single electron beaming angle: $\Theta_{\rm SR} \gg \Theta_1$. As such, the bunch radiates as a one-dimensional pencil beam, and the coherent amplification can only be increased by the quality of microbunching, the number of electrons per microbunch or the interaction length.

On the other hand, in the beer-can beam regime, destructive interference due to the finite waist of the bunch limits superradiant x-ray emission. If so, the opening angle of the superradiant cone is much smaller than the single electron emission angle; $\Theta_{\rm SR} \ll \Theta_1$, such that only a small part of the single electron scattering is effectively amplified. Here, we want to stress that for typical ICS parameters, the electron beam can be considered thick: taking the same example as in section 2, ($\lambda_X = 1.24$ nm, $\lambda_0 = 1032$ nm, $\gamma = 14$, $\sigma_\perp = 5\ \mu$m) and assuming a laser pulse length of 1 ps ($N_\phi \simeq 1.8 \times 10^3$) and $N_{\rm b} = 10^4$ microbunches. The collectivity parameter for this case amounts to $\xi = 1.1 \times 10^{-3}$ corresponding to a yield $\eta = 6.2 \times 10^{-4}$.

Focusing the electron beam more tightly should increase the superradiant flux, since $\xi \propto \sigma_\perp^{-2}$. Realistically, however, focusing to a waist smaller than a micron becomes difficult for several reasons. To start, tight focusing increases the transverse angular spread $\Theta_{\rm e}$ of the electron beam to a degree that the cold beam approximation becomes invalid. Effectively, the angular spread expands the opening angle when $\Theta_{\rm e} \geqslant \Theta_1$, counteracting the effect of the smaller waist, see later section 5. Furthermore, high electron density in the waist leads to an increase of the Coulomb forces, which are detrimental to yield, especially at low electron beam energies and the bunch charge required for ICS. Limitation in the production of superradiant x-rays due to Coulomb forces can be split up in two effects: first, the defocussing force due to self fields limits the smallest attainable waist. Second, the Coulomb forces in such foci degrade the intricate density modulation (b_1) within the beam.

A higher electron beam energy improves the overlap between the opening angles, while simultaneously reducing Coulomb forces. However, to attain resonance at a certain scattered wavelength, the frequency k_0 has to be reduced in head-on scattering. Figure 4 presents the superradiant yield η around $\lambda_X = 1.24$ nm, ($U_{\rm ph} = 1$ keV) for different values of Lorentz factor γ. The graph clearly shows that the superradiant yield from a typical electron beam with $\sigma_\perp = 5\ \mu$m waist at low beam energies (5–14 MeV), corresponding to a drive laser in the visible regime ($\lambda_0 = 400$–1000 nm, indicated by the grey box), is correctly described by a beer-can beam approximation (blue line). Therefore, the yield is significantly suppressed compared with a fully superradiant beam (red line). Note that equation (15), plotted with the solid black line is identical to numerical integration of (13) (green dashed line).

The transition to the pencil beam regime occurs at the energy when the yields for $\xi \gg 1$ (red line) and $\xi \ll 1$ (blue line) are equal. This happens when $\xi = \sqrt{\pi}$, or:

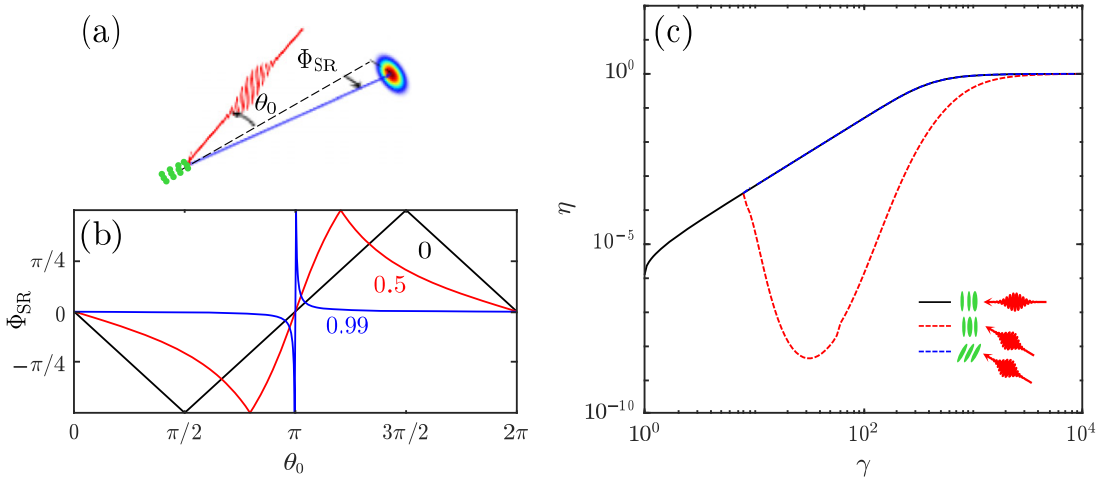

Figure 5. (a) Oblique incidence of the driving laser results in a walk-off angle of the superradiant emission. (b) Walk-off angle Φ_{SR} plotted against angle of incidence θ_0 for different values of normalized velocity β. (c) Superradiant yield for $\lambda_X = 4.1$ nm ($U_{ph} = 0.3$ keV) from a modulated Gaussian electron beam with $\sigma_\perp = 10$ μm and $N_b = 10^4$ microbunches a for head-on (black) non-collinear (red), and non-collinear scattering with micronbunch tilt (blue) with a $N_\phi = 10^3$ laser pulse.

$$\gamma_{tr} = \left(\frac{\pi}{4}\right)^{1/4} \frac{1}{\Theta_{SR}} \sqrt{\frac{\delta k}{k}}, \tag{18}$$

which for the parameters in figure 4 is at $U_{kin} = 386$ MeV. Electron beam energies near the transition energy are favorable for the yield. However, the resonant laser wavelength around γ_{tr} is on the millimeter scale, far from the visible regime.

4.2. Non-collinear scattering

In the previous section it was shown that the transverse size of the microbunches significantly limits the yield η at low electron beam energies required for head-on scattering using an optical laser. It was also shown that for a constant on-axis scattered frequency k_X, an increase of beam energy significantly increases the number of superradiant photons. At beam energies around the transition energy, however, the required wavelength of the driving wave is longer than visible wavelengths for the head-on geometry. Another way to control the scattered frequency (1), which allows the usage of visible lasers even at high beam energy, is to change the propagation direction $\mathbf{n}_0$ of the laser pulse in respect to the velocity of the electrons. However, if $\mathbf{n}_0$ does not coincide with the propagation and thus scattering axis of the electron bunch, extra transverse terms turn up in phase (9) such that the superradiant emission cone is redirected off-axis as illustrated in figure 5(a). For an electron bunch that is modulated longitudinally $\mathbf{k}_e = k_e \mathbf{e}_z$, the so-called walk-off angle of the superradiant cone can be inferred from equation (12), and is given by

$$\Phi_{SR} = \arcsin\left(\frac{(\beta^2 - 1)\sin\theta_0}{\sin^2\theta_0 + (\beta + \cos\theta_0)^2}\right), \tag{19}$$

where $\theta_0 = \arccos(-\mathbf{v}\cdot\mathbf{n}_0/v)$ the angle between propagation axis of the laser ($\mathbf{n}_0 = -\sin\theta_0\mathbf{e}_y - \cos\theta_0\mathbf{e}_z$) and electrons. Φ_{SR} can be thought of as the angle of specular reflection from a relativistic mirror, and is plotted against laser angle θ_0 for different values of β in figure 5(b). The maximum walk-off angle $\Phi_{SR,\,max} = \pi/2$ is found at laser angle $\theta_{0,max} = \arccos[-2\beta/(1+\beta^2)]$. In the ultrarelativistic regime, the walk-off angle $\Phi_{SR} \simeq -\tan(\theta_0/2)/(2\gamma^2)$ is small for $\theta_0 < \theta_{0,max} \simeq \pi$. However, as seen in figure 5(c), when $\Phi_{SR} \sim \Theta_1$, the shift in the direction of the superradiant cone leads to further loss of superradiant photons (red dashed line) with respect to the head-on scattering (black line).

There are several ways to compensate for this effect. First, adjusting the bunching frequency to match the resonant frequency along this angle $k_e = k_0(\cos\Phi_{SR} + \cos\theta_0)/(1 - \beta\cos\Phi_{SR})$ leads to an off-axis superradiant beam, which might be interesting for non-invasive monitoring of microbunching. Second, equation (19) suggests the walk-off angle becomes small again at high beam energies, ensuring that that $\Phi_{SR} < \Theta_1$, which results in a relative growth in number of photons. Third, two lasers can be used with θ_0 and $-\theta_0$: the superposed fields of the lasers in the interaction region form a wave with phase $\varphi = k_0 z\cos\theta_0 - \omega_0 t$, ensuring a wavefront that is aligned with the transverse plane of the electron bunch, such that no additional phase differences occur in the transverse plane. The bunching frequency using two lasers should match the on-axis resonance frequency as with a single laser pulse

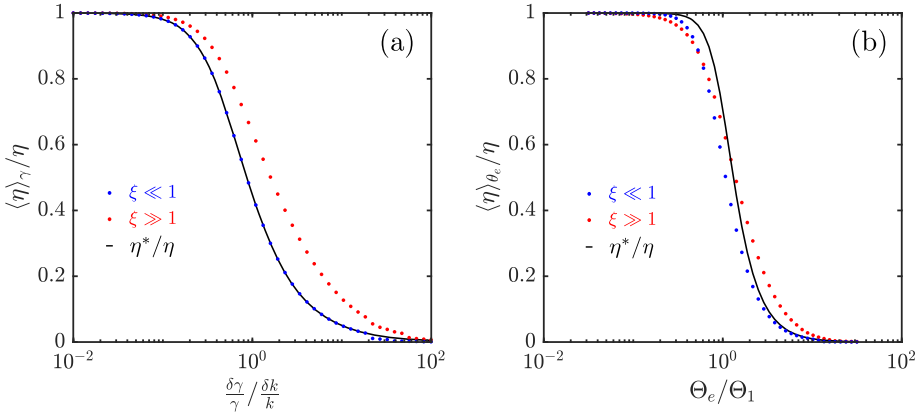

Figure 6. Yield normalized to cold-beam yield including: (a) energy spread and (b) angular spread from head-on scattering at $\gamma = 14$ with $\delta k/k = \sqrt{2}\,10^{-3}$. $\langle\eta\rangle_{\gamma,\theta_e}$ is the yield as calculated by numerical integration of the integral defined in appendix C.

$k_e = k_0(1+\cos\theta_0)/(1-\beta)$. Finally, a microbunch tilt can be applied such that $\mathbf{k}_e = k_e \sin\alpha\mathbf{e}_y + k_e\cos\alpha\mathbf{e}_z$, with α is the microbunch tilt angle. Microbunch tilts have been shown to form when a density modulated electron beam is simultaneously diverted and defocused [46]. The tilt angle that ensures on-axis superradiant radiation from ICS with a driving laser under an angle θ_0 can also be found from the bunching factor (12), and is given by $\alpha = \arctan[(1-\beta)\sin\theta_0/(1+\cos\theta_0)]$. A bunching frequency resonant with the on-axis frequency was used $k_e = k_0(1+\cos\theta_0)/(1-\beta)\sqrt{1+(1-\beta)^2\tan^2(\theta_0/2)}$, which is higher than the bunching frequency for non-tilted modulation. In figure 5(c) the numerically calculated superradiant yield is shown for tilted microbunches (blue dashed), which we find to follow equation (15) with $k_X = k_0(1+\beta\cos\theta_0)/(1-\beta)$.

5. Energy spread and angular spread

Until now we have assumed a perfectly cold electron beam. In reality, however, an electron beam has finite energy spread $\delta\gamma$ and transverse angular spread Θ_e, which can alter the radiation distribution so that the cold-beam approximation does not hold. Here, we numerically calculate (see appendix C) the superradiant yield under influence of energy spread and angular spread separately, the results of which are shown by the dots in figures 6(a) and (b) respectively. Also, a heuristic approach is presented to estimate the effect of energy and angular spread.

Due to energy spread each electron, and its generated radiation, experiences slightly different Doppler shifts, resulting in broadening of the (incoherent) ICS bandwidth by $(\delta k/k)_\gamma = 2\delta\gamma/\gamma$ [47, 48]. Bandwidth broadening leads to decrease of photons available for coherent amplification. When $\delta\gamma/\gamma \ll \delta k/k$, where $\delta k/k = \sqrt{1/N_b^2 + 1/N_\phi^2}$ the relevant cold beam bandwidth, we find that the induced frequency shift by energy spread is small enough that the superradiant yield remains unaffected. In this regime the cold beam approximation is appropriate, and the yield is correctly described by equation (15). Around $\delta\gamma/\gamma \simeq \delta k/k$ the difference in electron energy becomes significant and the yield drops by half. For $\delta\gamma/\gamma \gg \delta k/k$, the yields is significantly limited by the energy spread of the electrons.

Angular spread also induces broadening by $(\delta k/k)_{\theta_e} = \gamma^2\Theta_e^2$ of the Compton bandwidth [47, 48], mainly caused by the change in emission angle, which can hinder the efficiency of superradiant emission. When $\Theta_e \ll \Theta_1$, however, the effect of angular spread on the yield is insignificant. At $\Theta_e \simeq \Theta_1$, the angular spread becomes important and the yield has dropped to half of its cold beam value. For $\Theta_e \gg \Theta_1$ the superradiant yield is hindered significantly by angular spread of the electrons.

A secondary effect of finite angular spread is that the waist of the electron beam is changing along the beamline. A larger waist size leads to smaller Θ_{SR} and, for a beer-can beam, thus reduction of yield. The electron beam waist can be considered constant during interaction if the angular spread:

$$\Theta_e < \frac{k_0\sigma_\perp}{N_\phi}(1+\beta\,\cos\,\theta_0)\,, \tag{20}$$

where it is assumed here that the Rayleigh length of the laser is much longer than the pulse length so that the experienced intensity distribution is defined by the latter. For counterpropagating scattering geometries, the effect of the changing waist is typically less apparent than the spectral broadening effect from the

angular spread. However, when comoving laser pulses are used, the interaction length is extended, and the changing waist of the electron bunch might affect the superradiant yield more than the angular spread itself.

5.1. Estimation of superradiant yield

The combined effect of energy and angular spread on the relevant bandwidth of the scattered radiation can be written as:

$$\frac{\delta k^*}{k} = \sqrt{\frac{1}{N_\phi^2} + \frac{1}{N_\mathrm{b}^2} + \left(2\frac{\delta\gamma}{\gamma}\right)^2 + \gamma^4\Theta_\mathrm{e}^4}. \tag{21}$$

Due to the thermal spread of the electrons, the induced radiation angle $\Theta^* = \sqrt{\delta k^*/k}/\gamma$ becomes larger than the single electron radiation angle Θ_1. If equation (20) holds, Θ_{SR} will not change appreciably. Therefore, by naive substitution of $\Theta_1 \rightarrow \Theta^*$ in equations (16) and (17), we find that, in the beer-can beam regime, the superradiant yield from a bunch with a thermal distribution can be written as

$$\eta^* \simeq \frac{\frac{\delta k}{k}}{\frac{\delta k^*}{k}}\eta, \tag{22}$$

where $\delta k/k$ is the cold bandwidth. Especially for energy spread in the beer-can beam regime ($\xi \ll 1$) there is very good agreement of η^* with the results from numerical integration in figure 6(a). Furthermore, even for a pencil beam with energy or angular spread, equation (22) is a fair indication of the yield.

6. Application to source design: coldlight

To illustrate the use of previous expressions, we apply them to coldlight, which is a proposed superradiant soft x-ray source [49]. The source will be driven by microbunched electrons extracted from an ultracold electron source [50]. The electron source is a perfect ICS driver, since it has the unique property of allowing $Q \simeq 1$ pC electron bunches to be extracted while maintaining ultralow $\epsilon_n = 1$ nm rad transverse emittance, by minimization of the space charge forces due to the large ionization volume. In addition, the electron source lends unique control of the photoionization process: by exciting the laser cooled and trapped atoms using a standing wave of light, an electron bunch with about $N_\mathrm{b} = 1.25 \times 10^4$ microbunches can be generated with cosine density modulation $b_1 = 1/2$. After acceleration and compression, the electron bunch attains modulation at extreme ultraviolet to soft x-ray wavelength.

A particular interesting bandwidth within the soft x-ray regime is the water window, which is between $U_\mathrm{ph} = 282$–533 eV ($\lambda_X = 4.4$–2.3 nm). In this regime, water is transparent and carbon is absorbing, which is interesting for high contrast imaging in life sciences. Suppose we want to generate as much photons as possible for an advanced water window microscopy tool using a conventional 1 ps laser pulse of $\lambda_0 = 1$ μm with $A_0 = 0.1$. Using (4) it is found that potentially $N^{\mathrm{SR}}_{\mathrm{ph,\,1D}} = 8.1 \times 10^7$ can be generated with a $Q = 1$ pC electron bunch.

To reach the water window, a 3.5 MeV electron beam is required for head-on scattering. Due to the ultracold nature of the electrons, energy spread nor emittance will influence the yield. However, we estimate that, at this energy, the electron beam waist size should be not be focussed smaller than $\sigma_\perp = 5$ μm before the onset of significant debunching and increase of angular spread due to Coulomb forces. In such a scattering geometry we find that the superradiant efficiency $\eta = 2.2 \times 10^{-3}$, severely limiting the yield.

Alternatively, by accelerating the electrons to 35 MeV and introducing a non-colinear geometry, one can increase the flux by two orders of magnitude, since $\xi \propto \gamma^2$. Such energies can be reached with table top-accelerators [7]. Coulomb forces, scaling with γ^{-2}, reduce so that smaller waists can be attained without destroying the bunching, thereby further increasing the yield. Assuming the electron beam can be focused to $\sigma_\perp = 1$ μm at this higher energy, the superradiant yield is $N^{\mathrm{SR}}_{\mathrm{ph}} = 7 \times 10^7$, very close to full superradiant potential. However, in this regime $\Phi_{\mathrm{SR}} \sim \Theta_1$, so one of the walk-off angle compensating techniques should be applied. Without, we find through numerical calculation that the yield reduces by a factor of 5.

When operating at $f = 1$ kHz repetition rate, the average brightness of coldlight $B = fN^{\mathrm{SR}}_{\mathrm{ph}}/(\sigma_\perp\Theta_{\mathrm{SR}})^2 = 1.6 \times 10^{14}$ ph/(s · mm · mrad 0.1%BW), comparable to bending magnet radiation in a synchtrotron, is more than sufficient for water window microscopy [51] or coherent diffractive imaging techniques [52, 53]. Compact high brightness (soft) x-ray sources like coldlight are of great importance because they allow for easy integration with complementary imaging techniques, result in wide spread availability and lead to increase of beam time.

7. Conclusion

The superradiant x-ray yield from microbunched electrons depends not only on the quality of microbunching, but also strongly on the shape, beam energy, energy spread and angular spread of the macrobunch and scattering geometry. Summarizing, the number of superradiant emitted photons by a Gaussian shaped electron bunch with arbitrary density modulation is given by:

$$N_{\mathrm{ph}}^{\mathrm{SR}} = \frac{\pi}{4}\alpha A_0^2 N_\phi N_{\mathrm{e}}^2 \frac{b_n^2}{nN_{\mathrm{b}}} \mathrm{erfcx}\left(\frac{\Theta_1^2}{2\Theta_{\mathrm{SR}}^2}\right)\left[1+\left(\frac{2\delta\gamma}{\gamma^3\Theta_1^2}\right)^2+\frac{\Theta_{\mathrm{e}}^4}{\Theta_1^4}\right]^{-1/2}, \tag{23}$$

where we included superradiance from harmonics of the density modulation by substituting $N_{\mathrm{b}} \to nN_{\mathrm{b}}$. In equation (23), it is assumed that the scattering angle is small ($\Theta_{\mathrm{SR}} \ll 1$ or $\Theta_1 \ll 1$), the electron bunch consist of a multitude of microbunches ($N_{\mathrm{b}} \gg 1$), the laser pulse has a slowly varying envelope ($N_\phi \gg 1$), the laser waist is much larger than the electron beam waist and the laser field is not so intense ($A_0 \ll 1$) that non-linear scattering occurs. Additionally, the electron recoil is assumed to be negligible ($\gamma\hbar\omega_0/(m_{\mathrm{e}}c^2) \ll 1$). The expression holds for head-on scattering with on resonance bunching frequency $k_{\mathrm{e}} = k_0/(n(1-\beta))$ and for non-colinear scattering if the walk-off angle Φ_{SR} is compensated for. Including walk-off, equation (23) is a good approximation for the yield as long as $\Phi_{\mathrm{SR}} < \Theta_1$. Furthermore, the term between square brackets is not exact, but estimates of the influence of energy spread and angular spread.

Our main conclusion, based on equation (23), is that for electron beams of few MeV, the x-ray yield from head-on scattering with a visible laser is suppressed significantly if the waist is on the order of micrometers, since the opening angle of the diffraction cone of the superradiant beam is much smaller than the single electron opening angle. By increasing the energy, and introducing an oblique scattering geometry, more of the potential superradiance can be utilized, but only if one takes care of the walk-off angle. This is confirmed, by applying the expressions to a proposed coherent soft x-ray source.

Under certain conditions, the superradiant regime will transition to a FEL regime where the bunching factor amplitude b_n increases due to ponderomotive force from the beat wave formed by the laser pulse and ICS radiation. The stimulated superradiance in this regime can even further enhance the yield. In comparison to a SASE optical FEL starting from incoherent Compon scattering [11–13], superradiance from a prebunched beam could significantly decrease the saturation length L_{sat} of the FEL at which the radiation reaches its maximum intensity [54, 55]. Future work should point out if $L_{\mathrm{sat}} \propto -\ln(b_1^2)$ from one-dimensional high gain analysis [56], still holds in the beer-can beam regime, where speculatively the effective bunching factor amplitude $b_{\mathrm{eff}} \simeq b_1\Theta_{\mathrm{SR}}/\Theta_1$. If the latter is true, also in the (optical) FEL regime the preferred scattering geometry is non-collinear at higher electron beam energy as proposed in [13].

All in all, this work has provided essential insight in the relevant parameter space for superradiant ICS, which is of great importance for future high brightness, compact x-ray sources.

Acknowledgments

This research was funded by the Ministry of Economic Affairs in the Netherlands through a TKI-grant.

Data availability statement

All data that support the findings of this study are included within the article (and any supplementary files).

Appendix A. Single electron radiation distribution

A.1. Single electron photon intensity distribution

We describe the interaction between an electron and a laser pulse in the framework of covariant electrodynamics, using the metric $g^{\mu\nu} = \mathrm{diag}(1,-1,-1,-1)$. In this classical description we neglect electron recoil, restricting the initial laser frequency ω_0 to fulfill the condition $\gamma_0\hbar\omega_0/(m_{\mathrm{e}}c^2) \ll 1$, where γ_0 is the Lorentz factor of the electron prior to interaction, $\hbar$ the reduced Planck's constant, c the speed of light and m_{e} the electron mass. Furthermore, we restrict our discussion to the linear regime where the vector potential amplitude of the laser pulse A satisfies $eA/m_{\mathrm{e}}c \ll 1$, with e the elementary charge. In the linear regime the transverse momentum induced by the laser remains non-relativistic, which is desired in most experimental conditions to avoid spectral broadening. From here, unless stated otherwise, we will normalize the relevant parameters as follows: charge is measured in units e, mass in units m_{e}, time is measured in ω_0^{-1} of the initial laser frequency, length in $k_0^{-1} = c(\omega_0)^{-1}$ and (consequently) velocity is measured in units of c. In classical electrodynamics, the photon spectral density scattered into the far field is given by [30]

$$N_{k,\Omega}(\mathbf{k}) = -\alpha k \tilde{j}^{\mu} \tilde{j}_{\mu}, \tag{A.1}$$

where $\alpha = e^2/(4\pi\epsilon_0\hbar c)$ the fine-structure constant and $\tilde{j}^{\mu}(k)$ the four dimensional Fourier transform of the four current. For an electron the spectral four current is:

$$\tilde{j}^{\mu}(k) = -\frac{1}{2\pi}\int \mathrm{d}\tau\, u^{\mu}(\tau)\exp[ik^{\nu}x_{\nu}(\tau)], \tag{A.2}$$

where τ is the propertime of the electron, $u^{\mu}(\tau) = (\gamma, \gamma\boldsymbol{\beta})$ the four-velocity, with $\boldsymbol{\beta}$ the velocity vector, $x^{\mu}(\tau) = (t, \mathbf{x})$ the four-position and $k^{\mu} = (k, \mathbf{k})$ the four-wavevector of the scattered radiation. Equations (A.1) and (A.2) show that the electron's motion in the laser pulse fully determines the spectral angular radiation properties in the far field.

Neglecting radiation damping, the electron motion is described by the Lorentz force equation:

$$\frac{\mathrm{d}u^{\mu}(\tau)}{\mathrm{d}\tau} = u_{\nu}\left(\partial^{\nu}A^{\mu} - \partial^{\mu}A^{\nu}\right), \tag{A.3}$$

where $A^{\mu} = A^{\mu}(\varphi)$ is the four-potential describing the field of laser pulse with $\varphi = k_0^{\nu}x_{\nu}$ the optical phase and $k_0^{\mu} = (1, \mathbf{n}_0)$ the wavevector and $\mathbf{n}_0$ its propagation direction. If the Lorentz gauge condition $\partial^{\nu}A_{\nu} = 0$ holds and the vector potential only depends on φ, the exact solution to equation (A.3) is written as [45]

$$u^{\mu}(\tau) = u_0^{\mu} + A^{\mu}(\varphi) - \frac{1}{u_0^{v}k_{0v}}\left[\frac{1}{2}A^{\nu}A_{\nu}(\varphi) + u_0^{v}A_{v}(\varphi)\right]k_0^{\mu}, \tag{A.4}$$

where $u_0^{\mu} = (\gamma_0, \gamma_0\boldsymbol{\beta}_0)$ is the initial four-velocity. The second term here describes the quiver momentum induced by the laser pulse. The terms within brackets describe the momentum resulting from the ponderomotive force and a magnetic quiver motion respectively. Since the maximum amplitude of the four-potential $A_0 \ll 1$, the second order ponderomotive term is considerably smaller than the others, such that it can be neglected in the following. For sake of clarity, we choose the laser polarization perpendicular to the initial velocity, making the last term zero. This simplification does not deprive our model of any useful physics, but it makes the expressions much easier to compute. Furthermore, if the vector potential $A^{\mu} = A_0 f(\varphi)\mathrm{e}^{-\mathrm{i}\varphi}\epsilon^{\mu}$, where $\epsilon^{\mu} = (0, \epsilon)$ is the four-polarization, has a slowly varying amplitude, i.e. $\mathrm{d}f(\varphi)/\mathrm{d}\varphi \ll f(\varphi)$, we can integrate equation (A.4):

$$x^{\mu}(\varphi) \simeq x_0^{\mu} + u_0^{\mu}\tau + \frac{iA^{\mu}(\varphi)}{u_0^{\nu}k_{0\nu}}, \tag{A.5}$$

where we make use of the fact that $\mathrm{d}\varphi/\mathrm{d}\tau = k_0^{\nu}u_{\nu} = k_0^{\nu}u_{0\nu}$ is a constant of motion. Here, x_0^{μ} is the initial four-position of the electron in respect to the laser phase. The second term describes the uniform motion by the initial velocity of the electron. The last accounts for the quiver motion with an amplitude that is proportional to the time the electron propagates trough an optical cycle. It is important to note here that x^{μ} depends on φ and therefore it is a recursive relation, which we must readdress for a correct description of the bunching factor later on.

Equations (A.4) and (A.5) are now used to calculate the spectral four current. Before integrating equation (A.2), we expand the exponent to first order in A^{μ} by substituting equation (A.5):

$$\exp[ik^{\nu}x_{\nu}(\tau)] \simeq b_1\left[1 - \frac{k^{\mu}A_{\mu}(\varphi)}{u_0^{\nu}k_{0\nu}}\right]\exp(ik^{\nu}u_{0\nu}\tau), \tag{A.6}$$

where $b_1 = \exp(ik^{\nu}x_{0\nu})$ is the single electron phase factor. Higher orders of the expansion will contribute to higher harmonics, which do not contribute to the radiation in the linear regime. The Taylor expansion in (A.6) is identical to first performing the familiar Jacobi–Anger expansion and subsequently expanding the Bessel functions for small arguments.

Keeping only the terms that will contribute to the fundamental frequency, we find that:

$$\tilde{j}^{\mu}(k) = -b_1\left[\epsilon^{\mu} - \frac{k^{\nu}\epsilon_{\nu}}{u_0^{\nu}k_{0\nu}}u_0^{\mu}\right]\tilde{A}(k), \tag{A.7}$$

where

$$\tilde{A}(k) = \frac{A_0}{4\pi}\int \mathrm{d}\tau\, f(\varphi)\exp[i(k^{\nu} - k_0^{\nu})u_{0\nu}\tau], \tag{A.8}$$

is the Fourier transform of the amplitude of the laser pulse. In equation (A.8) a factor half is included to account for the fact that the laser field must be real valued. For a Gaussian pulse $f(\varphi) = \exp[-\frac{1}{2}(\varphi/N_\phi)^2] = \exp[-\frac{1}{2}(k_0^\nu u_{0\nu}\tau/N_\phi)^2]$, where in non-normalized units the number of oscillations in an rms pulse length $N_\phi = \omega_0\sigma_t$, with σ_t the rms pulse length as measured in the lab frame, the Fourier transform becomes:

$$\tilde{A}(k) = \frac{A_0 N_\phi}{2\sqrt{2\pi}k_0^\nu u_{0\nu}} \exp\left[-\frac{N_\phi^2}{2}\left(\frac{k^\nu u_{0\nu}}{k_0^\nu u_{0\nu}} - 1\right)^2\right]. \tag{A.9}$$

For most part, the function $\tilde{A}(k)$ describes the spectral properties of the radiation and will be referred to as the resonance function. The resonance function peaks when $k^\nu u_{0\nu} = k_0^\nu u_{0\nu}$, i.e. when the scattered frequency follows the well-known relation:

$$k = k_1 \equiv \frac{1 - \mathbf{n}_0 \cdot \boldsymbol{\beta}_0}{1 - \mathbf{n} \cdot \boldsymbol{\beta}_0}, \tag{A.10}$$

which is largest in the propagation direction of the electron, and becomes progressively lower going off axis. Here $\mathbf{n} = \mathbf{k}/k$ is the unit vector in the propagation direction of the scattered radiation. Away from resonance, the function $A(k)$ decays quickly when $N_\phi \gg 1$.

The radiation distribution (A.1) can now be easily calculated by contracting the four-current (A.7), resulting in the sought after expression.

Appendix B. Yield integral head-on scattering

For polarization $\boldsymbol{\epsilon} = \mathbf{e}_x$ and head-on propagation direction $\mathbf{n}_0 = -\mathbf{e}_z$, the yield integral (13) in spherical coordinates, can be written in the form

$$N_{\mathrm{ph}}^{\mathrm{SR}} = N_{\mathrm{e}}^2 L_0 \int \mathrm{d}\Omega \int_{-\infty}^{\infty} \mathrm{d}k \frac{k}{\kappa_0^2}\left[1 - \frac{k^2}{\kappa_0^2}\sin^2\theta\cos^2\phi\right] \exp\left[-Ak^2 + Bk + C\right], \tag{B.1}$$

where $L_0 = \alpha A_0^2 N_\phi^2/(4\pi)$ and $\kappa_0 = k_0\gamma(1+\beta)$ and coefficients

$$A = \sigma_\perp^2 \sin^2\theta + \sigma_\parallel^2 \frac{(1+\cos\theta)^2}{(1+\beta)^2} + N_\phi^2 \frac{(1-\beta\cos\theta)^2}{k_0^2(1+\beta)^2}, \tag{B.2}$$

$$B = \frac{2}{k_0(1+\beta)}\left[k_0 k_{\mathrm{e}}\sigma_\parallel^2 + N_\phi^2 + (k_0 k_{\mathrm{e}}\sigma_\parallel^2 - \beta N_\phi^2)\cos\theta\right], \tag{B.3}$$

$$C = -k_{\mathrm{e}}^2\sigma_\parallel^2 - N_\phi^2. \tag{B.4}$$

We can make use of the standard Gaussian integral $\int_{-\infty}^{\infty} \exp[-Ax^2 + Bx + C]\mathrm{d}x = \sqrt{\pi/A}\,\exp[B^2/(4A)]$ and its derivatives to coefficients A and B to integrate and find:

$$N_{\mathrm{ph}}^{\mathrm{SR}} = \frac{\sqrt{\pi}N_{\mathrm{e}}^2 L_0}{2\kappa_0^2}\int_0^\pi \mathrm{d}\theta \int_0^{2\pi} \mathrm{d}\phi\, \sin\theta \left(\frac{B}{A^{3/2}} - \frac{2A + B^2}{4\kappa_0^2 A^{5/2}}\sin^2\theta\cos^2\phi\right)\exp\left[\frac{B^2}{4A} + C\right]. \tag{B.5}$$

Now, we assume that the superradiant emission is contained to a small angle and fill in $k_{\mathrm{e}} = 2k_0/(1-\beta)$ so that on-axis coherence is stimulated. Within the small angle approximation the terms of (B.1) can be written as:

$$\frac{B}{A^{3/2}}\sin\theta \simeq \left(\frac{1+\beta}{1-\beta}\right)^2 \frac{2\theta}{\sqrt{N_{\mathrm{b}}^2 + N_\phi^2}}, \tag{B.6}$$

$$\frac{2A + B^2}{4\kappa_0^2 A^{5/2}}\sin^3\theta\cos^2\phi \simeq 0, \tag{B.7}$$

$$\frac{B^2}{4A} + C \simeq -k_X^2\sigma_\perp^2\theta^2 - \left(\frac{1+\beta}{1-\beta}\right)^2 \frac{N_{\mathrm{b}}^2 N_\phi^2}{N_{\mathrm{b}}^2 + N_\phi^2}\frac{\theta^4}{16}, \tag{B.8}$$

where $N_{\mathrm{b}} = k_{\mathrm{e}}\sigma_\parallel = 2k_0\sigma_\parallel/(1-\beta)$ the number of microbunches. Filling (B.6)–(B.8) into equation (B.1) and integrating over scattering angle θ and azimuthal angle ϕ yields the sought after equation.

Appendix C. Yield integral thermal electron bunch

We check equation (22) by numerical integration of the superradiant yield (13) including energy and angular spread. First, we replace the velocity in the radiation distribution (7) and bunching factor (12) by $\mathbf{v} = c(\beta + \Delta\beta)(\theta_{e,x}\mathbf{e}_x + \theta_{e,y}\mathbf{e}_y + \sqrt{1 - \theta_{e,x}^2 - \theta_{e,y}^2}\mathbf{e}_z)$, where $\Delta\beta$ the deviation of the normalized velocity with respect to β, and $\theta_{e,x}$ and $\theta_{e,y}$ are the angles of incidence with respect to the average propagation axis of the electron bunch. Note that angular spread in this definition of $\mathbf{v}$ does not affect the energy of the electron beam. The influence on yield η is calculated by numerically evaluating the following integral:

$$\langle\eta\rangle_{\gamma,\theta_e} = \frac{\gamma^3}{\pi^{3/2}\Theta_e^2\delta\gamma}\int_{-\infty}^{\infty} \mathrm{d}(\Delta\beta)\mathrm{d}\theta_{e,x}\,\mathrm{d}\theta_{e,y}\eta\,\exp\left[-\gamma^6\frac{\Delta\beta^2}{\delta\gamma^2} - \frac{\theta_{e,x}^2 + \theta_{e,y}^2}{\Theta_e^2}\right], \tag{C.1}$$

where $\gamma = (1 - \beta^2)^{-1/2}$ is the average Lorentz factor and we assumed that $\delta\gamma \simeq \delta\beta\gamma^3$ with $\delta\beta$ the normalized velocity spread.

ORCID iDs

B H Schaap https://orcid.org/0000-0003-0561-8400
T D C de Vos https://orcid.org/0000-0002-0448-8854
O J Luiten https://orcid.org/0000-0003-2048-4455

References

[1] Seddon E A *et al* 2017 Short-wavelength free-electron laser sources and science: a review *Rep. Prog. Phys.* **80** 115901
[2] McNeil B W J and Thompson N R 2010 X-ray free-electron lasers *Nat. Photon.* **4** 814–21
[3] Huang N, Deng H, Liu B, Wang D and Zhao Z 2021 Features and futures of x-ray free-electron lasers *Innovation* **2** 100097
[4] Du Y *et al* 2013 Generation of first hard x-ray pulse at Tsinghua Thomson scattering x-ray source *Rev. Sci. Instrum.* **84** 053301
[5] Bacci A *et al* 2014 The star project *Proc. Int. Particle Accelerator Conf.* pp 2238–41
[6] Eggl E, Dierolf M, Achterhold K, Jud C, Günther B, Braig E, Gleich B and Pfeiffer F 2016 The Munich compact light source: initial performance measures *J. Synchrotron Radiat.* **23** 1137–42
[7] Stragier X F D, Mutsaers P H A and Luiten O J 2018 Smart* light: a tabletop, high brilliance, monochromatic and tunable hard x-ray source for imaging and analysis *Microsc. Microanal.* **24** 310–1
[8] Dupraz K *et al* 2020 The ThomX ICS source *Phys. Open* **5** 100051
[9] Dicke R H, Palmer P and Aboratory I 1954 Coherence in spontaneous radiation processes *Phys. Rev.* **93** 99
[10] Gover A 2005 Superradiant and stimulated-superradiant emission in prebunched electron-beam radiators: I. Formulation *Phys. Rev. Accel. Beams* **8** 030701
[11] Bacci A, Ferrario M, Maroli C, Petrillo V and Serafini L 2006 Transverse effects in the production of x rays with a free-electron laser based on an optical undulator *Phys. Rev. Accel. Beams* **9** 060704
[12] Bacci A, Maroli C, Petrillo V, Rossi A R, Serafini L and Tomassini P 2008 Compact x-ray free-electron laser based on an optical undulator *Nucl. Instrum. Methods Phys. Res.* A **587** 388–97
[13] Steiniger K, Albach D, Bussmann M, Loeser M, Pausch R, Röser F, Schramm U, Siebold M and Debus A 2019 Building an optical free-electron laser in the traveling-wave Thomson-scattering geometry *Front. Phys.* **6** 155
[14] Graves W S, Kärtner F X, Moncton D E and Piot P 2012 Intense superradiant x rays from a compact source using a nanocathode array and emittance exchange *Phys. Rev. Lett.* **108** 263904
[15] Nanni E A, Graves W S and Moncton D E 2018 Nanomodulated electron beams via electron diffraction and emittance exchange for coherent x-ray generation *Phys. Rev. Accel. Beams* **21** 014401
[16] Bonifacio R, De Salvo Souza L, Pierini P and Scharlemann E T 1990 Generation of XUV light by resonant frequency tripling in a two-wiggler FEL amplifier *Nucl. Instrum. Methods Phys. Res.* A **296** 787–90
[17] Yu L H 1991 Generation of intense UV radiation by subharmonically seeded single-pass free-electron lasers *Phys. Rev.* A **44** 5178
[18] Yu L-H *et al* 2000 High-gain harmonic-generation free-electron laser *Science* **289** 932–4
[19] Xiang D and Stupakov G 2009 Echo-enabled harmonic generation free electron laser *Phys. Rev. Accel. Beams* **12** 030702
[20] Zhao Z T *et al* 2012 First lasing of an echo-enabled harmonic generation free-electron laser *Nat. Photon.* **6** 360–3
[21] Rebernik Ribič P *et al* 2019 Coherent soft x-ray pulses from an echo-enabled harmonic generation free-electron laser *Nat. Photon.* **13** 555–61
[22] Nguyen D C and Carlsten B E 1996 Amplified coherent emission from electron beams prebunched in a masked chicane *Nucl. Instrum. Methods Phys. Res.* A **375** 597–601
[23] Kozák M, Eckstein T, Schönenberger N and Hommelhoff P 2017 Inelastic ponderomotive scattering of electrons at a high-intensity optical travelling wave in vacuum *Nat. Phys.* **14** 121–5
[24] Moody J T, Li R K, Musumeci P, Scoby C M and To H 2012 Longitudinal phase space manipulation of an ultrashort electron beam via THz IFEL interaction *AIP Conf. Proc.* **1507** 722
[25] Priebe K E, Rathje C, Yalunin S V, Hohage T, Feist A, Schäfer S and Ropers C 2017 Attosecond electron pulse trains and quantum state reconstruction in ultrafast transmission electron microscopy *Nat. Photon.* **11** 793–7
[26] Kozák M *et al* 2017 Optical gating and streaking of free electrons with sub-optical cycle precision *Nat. Commun.* **8** 14342
[27] Boscolo M, Ferrario M, Boscolo I, Castelli F and Cialdi S 2007 Generation of short THz bunch trains in a RF photoinjector *Nucl. Instrum. Methods Phys. Res.* A **577** 409–16
[28] McCulloch A J, Putkunz C T, Sheludko D V, Nugent K A, Scholten R E and Saliba S D 2012 Spatial coherence of electron bunches extracted from an arbitrarily shaped cold atom electron source *Opt. Express* **20** 3967–74

[29] McCulloch A J, Sheludko D V, Junker M and Scholten R E 2013 High-coherence picosecond electron bunches from cold atoms *Nat. Commun.* **4** 1692
[30] Jackson J D 1998 *Classical Electrodynamics* 3rd edn (Hoboken, New Jersey: Wiley)
[31] Esarey E, Ride S K and Sprangle P 1993 Nonlinear Thomson scattering of intense laser pulses from beams and plasmas *Phys. Rev.* E **48** 3003
[32] Tomassini P, Giulietti A, Giulietti D and Gizzi L A 2005 Thomson backscattering x-rays from ultra-relativistic electron bunches and temporally shaped laser pulses *Appl. Phys.* B **80** 419–36
[33] Hartemann F V and Wu S S Q 2013 Nonlinear brightness optimization in Compton scattering *Phys. Rev. Lett.* **111** 044801
[34] Ghebregziabher I, Shadwick B A and Umstadter D 2013 Spectral bandwidth reduction of Thomson scattered light by pulse chirping *Phys. Rev. Accel. Beams* **16** 030705
[35] Terzić B, Deitrick K, Hofler A S and Krafft G A 2014 Narrow-band emission in Thomson sources operating in the high-field regime *Phys. Rev. Lett.* **112** 074801
[36] Rykovanov S G, Geddes C G R, Schroeder C B, Esarey E and Leemans W P 2016 Controlling the spectral shape of nonlinear Thomson scattering with proper laser chirping *Phys. Rev. Accel. Beams* **19** 030701
[37] Terzić B, Mckaig J, Johnson E, Dharanikota T and Krafft G A 2021 Laser chirping in inverse Compton sources at high electron beam energies and high laser intensities *Phys. Rev. Accel. Beams* **24** 094401
[38] Graves W S *et al* 2014 Compact x-ray source based on burst-mode inverse Compton scattering at 100 kHz *Phys. Rev. Accel. Beams* **17** 120701
[39] Toonen W F, Luiten X F D A, Stragier X F D, Mutsaers P H A and Luiten O J 2019 Gigahertz repetition rate thermionic electron gun concept *Phys. Rev. Accel. Beams* **22** 123401
[40] Coisson R 1986 Coherent and incoherent radiation from charged particle beams *Insertion Devices for Synchrotron Sources* vol 0582 pp 20–3
[41] Saldin E L, Schneidmiller E A and Yurkov M V 2005 A simple method for the determination of the structure of ultrashort relativistic electron bunches *Nucl. Instrum. Methods Phys. Res.* A **539** 499–526
[42] Saldin E L, Schneidmiller E A and Yurkov M V 2000 Diffraction effects in the self-amplified spontaneous emission FEL *Opt. Commun.* **186** 185–209
[43] Hirschmugl C J, Sagurton M and Williams G P 1991 Multiparticle coherence calculations for synchrotron-radiation emission *Phys. Rev.* A **44** 1316
[44] Ride S K, Esarey E and Baine M 1995 Thomson scattering of intense lasers from electron beams at arbitrary interaction angles *Phys. Rev.* E **52** 5425
[45] Hartemann F V, Baldis H A, Kerman A K, Le Foll A, Luhmann N C and Rupp B 2001 Three-dimensional theory of emittance in Compton scattering and x-ray protein crystallography *Phys. Rev.* E **64** 016501
[46] Macarthur J P, Lutman A A, Krzywinski J and Huang Z 2018 Microbunch rotation and coherent undulator radiation from a kicked electron beam *Phys. Rev.* X **8** 041036
[47] Curatolo C, Drebot I, Petrillo V and Serafini L 2017 Analytical description of photon beam phase spaces in inverse Compton scattering sources *Phys. Rev. Accel. Beams* **20** 080701
[48] Ranjan N, Terzić B, Krafft G A, Petrillo V, Drebot I and Serafini L 2018 Simulation of inverse Compton scattering and its implications on the scattered linewidth *Phys. Rev. Accel. Beams* **21** 030701
[49] Franssen J G H, Schaap B H, de Raadt T C H, Nijhof D F J, Mutsears P H A and Luiten O J 2019 From ultracold electrons to coherent soft x-rays (arXiv:1905.04031)
[50] Franssen J G H, De Raadt T C H, Van Ninhuijs M A W and Luiten O J 2019 Compact ultracold electron source based on a grating magneto-optical trap *Phys. Rev. Accel. Beams* **22** 023401
[51] Kördel M *et al* 2020 Laboratory water-window x-ray microscopy *Optica* **7** 658–74
[52] Rosenhahn A, Giewekemeyer K, Beckers M, Grunze M, Gorniak T and Salditt T 2011 Ptychographic coherent x-ray diffractive imaging in the water window *Opt. Express* **19** 1037–50
[53] Rothhardt J, Tadesse G K, Eschen W and Limpert J 2018 Table-top nanoscale coherent imaging with XUV light *J. Opt.* **20** 113001
[54] Freund H P, Nguyen D C and Carlsten B 2012 Three-dimensional analysis of prebunched electron beams in an x-ray free-electron laser *Phys. Rev. Accel. Beams* **15** 030704
[55] Jia Q 2017 Analysis of emissions from prebunched electron beams *Phys. Rev. Accel. Beams* **20** 070702
[56] Nicola P and Volpe L 2021 A review of high-gain free-electron laser theory *Atoms* **9** 28